OPTIMIZATION AND CHARACTERIZATION OF NI-WC COMPOSITE WELD MATRIX DEPOSITED BY PLASMA-TRANSFERRED ARC PROCESS

ALI TAHAEI^A, PAUL HORLEY^B, MATTIA MERLIN^A, DAVID TORRES-TORRES^B,
GIAN LUCA GARAGNANI^A, ROLANDO PRAGA^C, FELIPE J. GARCÍA VÁZQUEZ^C,
AND ANA ARIZMENDI-MORQUECHO^{B,*}

^{A} DEPARTMENT OF ENGINEERING, UNIVERSITY OF FERRARA, VIA G. SARAGAT 1,
44122 FERRARA, ITALY

^{B} CENTRO DE INVESTIGACIÓN EN MATERIALES AVANZADOS S.C. (CIMAV), UNIDAD
MONTERREY, ALIANZA NORTE 202, 66628 PARQUE PIIT, NUEVO LEÓN, MEXICO

^{C} CORPORACIÓN MEXICANA DE INVESTIGACIÓN EN MATERIALES S.A. DE C.V.
(COMIMSA), CIENCIA Y TECNOLOGÍA 790, 25290 SALTILLO-400, COAHUILA, MEXICO

* CORRESPONDING AUTHOR: PHONE (+52 81) 1156 0811, E-MAIL:
ANA.ARIZMENDI@CIMAV.EDU.MX

ABSTRACT. This work is dedicated to optimization of carbide particle system in a weld bead deposited by PTAW technique over D2 tool steel with high chromium content. We report partial melting of the original carbide grains of the Ni-based filling powder, and growing of the secondary carbide phase $(Cr, Ni)_3W_3C$ in the form of dendrites with wide branches that enhanced mechanical properties of the weld. The optimization of bead parameters was made with design of experiment methodology complemented by a complex sample characterization including SEM, EDXS, XRD and nano-indentation measurements. It was shown that the pre-heat of the substrate to a moderate temperature (250°C) establishes linear pattern of metal flow in the weld pool, resulting in the most homogeneous distribution of the primary carbides in the microstructure of weld bead.

1. INTRODUCTION

Hardfacing by plasma transferred arc welding (PTAW) is widely used in deposition of wear-resistant coatings on to the surface of metals with applications ranging from machinery components operating under harsh working conditions up to aeronautical applications[1]. PTAW has many beneficial features: low cost, low heat input, high efficiency, easy operation, synchronized powder-feeding mechanism and automation simplicity[2, 3, 4, 5]. The most widely used materials for wear resistant overlays are nickel and iron-based powders mixed with tungsten carbide (WC) particles, providing M_7C_3 carbide phase during solidification. Nickel-based alloys allow achievement of better abrasion and corrosion resistance at reasonably low material/processing cost. The majority of WC phases in conventional hardfacing are eutectoid W_2C/WC particles with about 3.7-4.1 Wt% of carbon[2] with

ALI TAHAEI[A], PAUL HORLEY[B], MATTIA MERLIN[A], DAVID TORRES-TORRES[B], GIAN LUCA GARAGNANI[A], ROLANDO PR
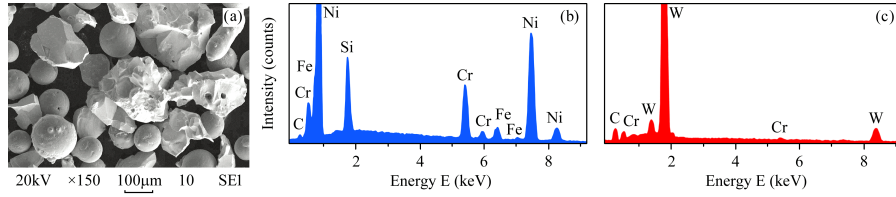

FIGURE 1. Morphology (a) and chemical composition of Ni-Cr-Si + WC hardfacing powder. The composition spectra were measured for a spherical Ni-Cr-Si grain (b) and irregular WC grain (c).

high combined impact/abrasion properties[6]. However, this phase has poor oxidation resistance under $T > 550°C$[7]. The dissolution of carbide particles favors formation of secondary phases, elongated tungsten-rich precipitates and a small concentration of W ending up in solid solution[8, 9]. Adding Cr (about 14 Wt%) to the matrix alloy causes a significant fraction of secondary carbides to precipitate during WC dissolution process[10, 11]. The major issues in achieving optimal performance of the Ni-WC composite overlays are non-uniform distribution and degradation/dissolution of the carbide particles. The importance of dilution is paramount, as it significantly alters the substrate properties and considerably reduces overlay wear resistance. The dilution in welds is directly related to the heat input during the welding process[6]. When depositing Ni-WC overlays, the settling of carbides produces a zone of low wear resistance on top of the hardfacing. Therefore, the final microstructure and phases are influenced by many technological parameters including welding current, nozzle travel speed and oscillation amplitude, substrate preheating and choice of a welding gas. Important studies had been dedicated to modeling and prediction of molten pool dimensions in PTAW process, aiming to understand the influence of deposition parameters (including weld bead width, height, dilution and aspect ratio)[3, 12, 13, 14, 15, 16, 17]. Despite of these achievements, the question of accurate control of weld bead geometry together with metallurgical behavior of the hardfacing layer lacks final refinement. The problem is essentially complicated by the need of control dissolution degree of the primary carbides and final distribution of WC grains in bead cross-section. The present paper offers a partial solution of these problems by using DOE with multi-parameter sample characterization aiming on optimization of PTAW hardfacing for nickel-based powder.

2. MATERIALS AND EXPERIMENTAL PROCEDURE

2.1. **Materials.** The nominal chemical composition (Wt%) of high-carbon D2 tool steel is summarized in Table 1. Prior to the welding, a standard tempering procedure was performed to improve hardness and toughness of the steel, heating the samples to 790°C during 1 hour, increasing the temperature to 1100°C for 35 minutes with further quenching in oil; after that, two additional tempering treatments were performed for 2 hours each at 315°C. The resulting tempered steel samples were cut into substrates with dimensions $130 \times 50 \times 12.5$ mm^3, further used for PTAW hardfacing. Before application of the overlay, the substrates were mechanically polished with SiC sandpaper to remove the oxide layer and macroscopic
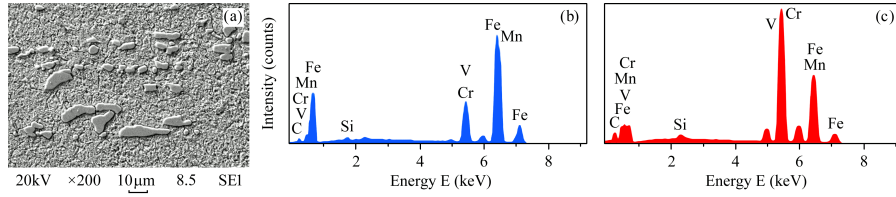
FIGURE 2. Morphology (a) and chemical composition of D2 tool steel substrate. The composition spectra are measured for steel matrix (b) and a large carbide grain (c).

TABLE 1. Nominal chemical composition (Wt%) of D2 tool steel and hardfacing powder alloy, including matrix and reinforcement carbide phases

Material	C	Si	Mn	Cr	Mo	V	P	S	B	W	Ni	Fe
D2 Steel	1.58	0.37	0.48	11.52	0.89	0.56	0.017	0.029	–	–	–	Bal.
Matrix	0.6-0.8	3.9-4.9	–	14.0-16.0	–	–	–	–	3.0-3.4	–	Bal.	–
Carbide	6.0-6.2	–	–	–	–	–	–	–	–	Bal.	–	–

surface contaminants proceeding from the tempering stage. The nominal chemical composition of Ni-WC powder alloy used for welding is listed in Table 1.

During the welding process the carbides of the substrate steel and those of the hardfacing powder interact in a certain way, so that it was important to have more information about the original composition and microstructure of the substrate and the filler mixture. As one can see from Fig. 1a, the hardfacing powder contains spherical particles of Ni-Cr-Si alloy (40%Vol.) intermixed with irregular tungsten carbide WC particles (60%Vol.), as listed by the provider (Table 1). In addition to this, we detected Fe in residual concentration of 4.35Wt% in hardfacing powder (Fig. 1b).

The micrographs of D2 steel substrate shown in Figure 2, revealing martensitic microstructure with scattered carbide grains of different size. The predominant original carbide in this system is $Cr_{23}C_6$; however, it dissolves during austenization process at the temperatures exceeding 900°C. The carbide structures seen in the tempered samples correspond mainly to the secondary chromium carbide Cr_7C_3, precipitating from the austenite phase and dispersed in the matrix[19]. The energy dispersive X-ray spectroscope (EDXS) analysis reports the presence of vanadium carbide phase (Fig. 2c). This is remarkable, as vanadium carbides VC and V_2C are hard and thermally stable[18], which will enhance wear and abrasive resistance of the material. Despite high mechanical resistance of carbides, their pronounced presence in D2 tool steel makes the material susceptible for cracking if operated under high pressures or elevated temperatures. Therefore, to widen the spectrum of possible applications, it will be highly beneficial to improve the mechanical properties of D2 steel especially for the harsh operating conditions. This problem that can be efficiently solved with hardfacing. Taking into account the distribution and morphology of carbide sub-system in the substrates, we opted for using PTAW technique as it offers finer control of process parameters and requires lower heat input, helpful for reducing undesirable cracking of the substrates.

2.2. **Experiment and characterization techniques.** We used PTAW equipment Castolin Eutectic Eutronic Gap 3001DC for applying the hardfacing layer over D2 tool steel samples. Due to a large number of process parameters influencing the size and the quality of resulting welding bead, we have chosen the ones that have major impact on bead formation: welding current I, nozzle travel speed V and sample pre-heat temperature T. This set of parameters was employed for design of experiment, allowing to reduce the number of the welding runs required to define the optimal deposition parameters. The other process parameters were fixed in all reported experiments as following: plasma voltage 20 V, nozzle diameter 3.2 mm, and torch to surface distance 10 mm. We used Ar as a plasma gas with a flow rate of 12 L/min, Ar+10%H_2 as a shielding gas with a flow rate of 3.5 L/min, and Ar as a carrier gas with a flow rate of 3.5 L/min. The filler powder feeding rate was 29 g/min. The equipment operated a robotic arm holding the welding torch.

After the welding, the samples were cut transversally and prepared for metallographic studies: polished with sand paper and diamond polisher with grain size varying from 6 to 1 μm. After achieving a mirror-like surface, the samples were subjected to chemical etching in 2% Nital, followed by the solution of 30% HF and 70% HNO_3. The visual study of the prepared samples was performed with Olympus SZX A0 stereomicroscope equipped with Infinity Analyze[TM]software for measurement of bead geometry parameters such as width, penetration, and reinforcement according to the commonly used methodology[20]. The Vickers microhardness test (HV) was performed with Micro-Hardness Tester Clemex MMT-X7, applying the indentation load of 300 gf for 10 s to produce series of indentation marks separated by 100 μm.

The microstructural analysis was performed with FEI Nova Nano SEM 200 system equipped with EDXS. The measurement results were analyzed with INCA[TM]software. The elastic modulus and hardness of the samples were determined with nano-indentation on TI 950 Triboindenter by Hysitron, equipped with the Berkovich diamond tip. The maximum applied load of 1 mN was used to characterize the softer phases, and 1.5 mN load was used for a harder WC phase. All nano-indentations were made with a loading-unloading rate of 150 μN/seg. Before the measurements, the surface of the samples achieved additional treatment with silicon carbide sandpaper, further with a commercial 500 nm diamond paste. We analyzed several phases seen on the sample cross-section, producing at least ten nano-indentations per phase area according to established measurement technique. The resulting load-penetration depth $(P - h)$ curves were used to calculate elastic modulus and hardness of the phases with the Oliver-Pharr method[21]. The crystallographic structure of hardfacing was studied with Brucker AXS D-8 XRD equipment, CuK$_\alpha$ ($\lambda = 0.154$nm) at 40kV and 20mA; XRD peak identification was made with Diffrac Plus[TM]software.

3. RESULTS AND DISCUSSION

3.1. **Optimization of bead geometry.** To reduce the number of experiments required for optimization of weld bead geometry, we used design of experiment technique with statistical analysis in Minitab[TM]software package. It should be emphasized that general optimization of bead geometry with all the multitude of control parameters offered by PTAW is much complicated, not only because requiring a large number of experiments but also due to the difficulty of finding the
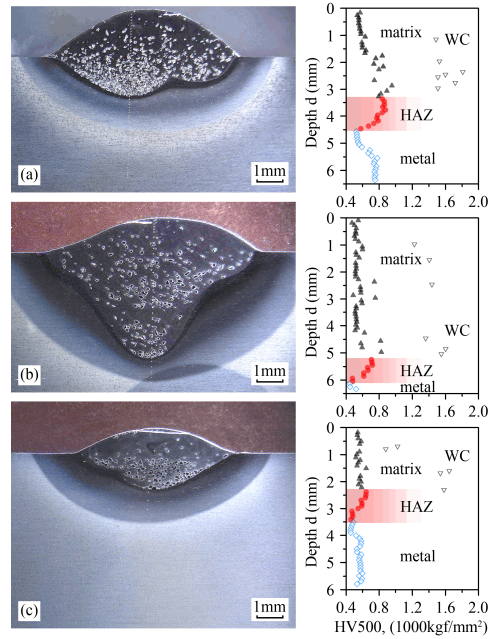
FIGURE 3. Macrostructure and hardness profiles of the characteristic bead samples obtained for the DOE matrix with: a) $I =$ 100A, $V = 70$cm/min, $T = 250°$C; b) $I = 140$A, $V = 70$cm/min, $T = 450°$C; and c) $I = 100$A, $V = 100$cm/min, $T = 450°$C.

corresponding extreme points in the multi-dimensional parameter space. Therefore, it is relevant to handle optimization problem with a moderate number of control parameters having the highest impact on the deposition process. Among these, it is imperative to consider the parameters controlling heat input and bead solidification rate: the welding current I (defining the amount of heat input) and the nozzle travel speed V (influencing heating/cooling rate). As D2 steel has high carbon and chromium content, it may be susceptible to crack formation during welding process. To reduce the thermal shock, we also considered the substrate pre-heat temperature T as one of control parameters.

In the selected three-parameter optimization problem, the DOE was used for the central composite rotatable matrix composed of 20 points: six center points, six star points and eight factorial design points. The proper intervals of parameter values were determined with series of preliminary experiments based on the technical data provided with the welding powder, resulting in the following ranges: variation of the current 100A $\leq I \leq$ 140A, nozzle travel speed 70cm/min $\leq V \leq$ 100cm/min and sample pre-heat 250°C $\leq T \leq$ 450°C. These intervals were normalized to -1 $\leq X_i \leq$ +1. The reduced value was calculated with the expression $X_i = [2X - (X_{max} + X_{min})]/(X_{max} - X_{min})$, using the maximum and minimum values provided for each control parameter. To ensure 90.75% confidence level for a normally-distributed variable, the interval was extended to enclose the critical values of two-sided Gaussian, producing the ranges -1.682 $\leq X_n \leq$ +1.682 that was used to define star points in the experimental design matrix. To avoid systematic errors,
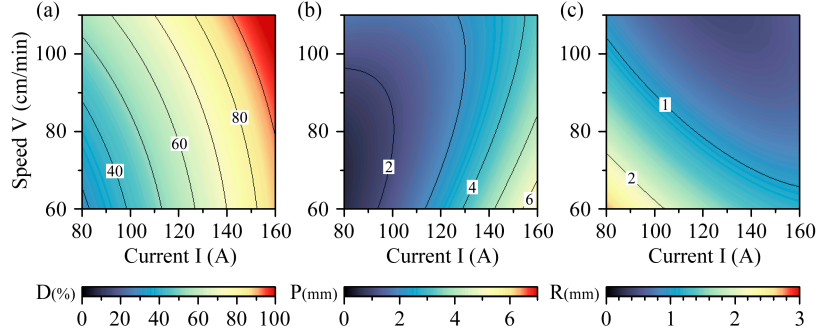
FIGURE 4. Dependence of a) dilution D, b) penetration P and c) reinforcement R on current I and travel speed V for the constant substrate pre-heat temperature $T = 250°$C.

the required 20 welding experiments were carried out in a random order. The resulting samples were characterized to define the main parameters of the weld bead including penetration depth P [mm], weld reinforcement R [mm] and dilution $D = P/(P + R)$ [%].

The characteristic cross-sections of weld beads corresponding to the DOE matrix are shown in Fig. 3. The hardness profiles shown in right panels were measured along the indentation lines visible in the macrographs. In all cases, no cracks were observed at the interface between the hardfacing layer and the base metal. As one can see from Fig. 3, WC grains are either clustered at the bottom of the welding bead (Fig. 3a, c) or homogeneously dispersed over its entire cross-section (Fig. 3b). The latter is definitely preferable distribution by providing more structural integrity to the hardfacing. However, the exact control over carbide grain configuration in the welding pool is one of the most complicated questions that will be addressed in detail for the optimized samples.

The geometry of the bead varies significantly with welding parameters. At the moderate welding currents the penetration is relatively small (Fig. 3a, c). Better reinforcement can be achieved for slower nozzle motion (Fig. 3a). The increasing heat input obtained with high welding current results in excess penetration and wide heat affected zone (Fig. 3b). The microhardness profiles show an abrupt hardness drop at the edge of the heat affected zone. The samples pre-heated to higher temperatures feature lower average hardness values (Fig. 3b, c): for $T = 250°$C (Fig. 3a) the average hardness of the bead matrix and carbide phases are 667 ± 123 HV and 1591 ± 106 HV, respectively. For $T = 450°$C (Fig. 3b) the average hardness for the same phases are 566 ± 78 HV and 1560 ± 201 HV, respectively.

The obtained parameters were analyzed with the statistical software package Minitab^{TM} to calculate the response surfaces in the form of second-order interpolation polynomials

(1) $$f(x_1, x_2, x_3) = b_0 + b_i x_i + b_{ii} x_i^2 + b_{ij} x_i x_j.$$

The summation is implied over the duplicate sub-indices in Eq. (1). The obtained polynomials for dilution, penetration and reinforcement are:
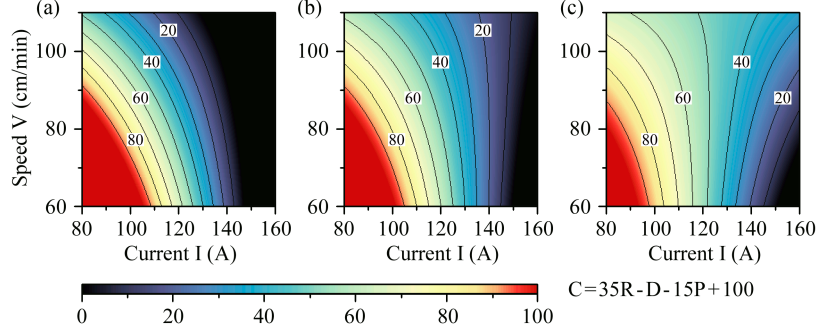
FIGURE 5. Dependence of a combined parameter $C = 35R - D - 15P + 100$ on current I and nozzle travel speed V for different substrate pre-heat temperatures: a) $T = 250°$C, b) $T = 350°$C, and c) $T = 450°$C.

$$(2) \quad \begin{aligned} D(I,V,T) = &-82 + 0.81I + 0.46V + 0.207T + 1.4 \times 10^{-3}I^2 \\ &+ 4 \times 10^{-3}V^2 + 3.7 \times 10^{-5}T^2 - 2.4 \times 10^{-3}IV \\ &- 1.05 \times 10^{-3}IT - 1.71 \times 10^{-3}VT, \end{aligned}$$

$$(3) \quad \begin{aligned} P(I,V,T) = &-4.48 + 3.61 \times 10^{-2}I + 9 \times 10^{-3}V + 1.35 \times 10^{-2}T \\ &+ 3.83 \times 10^{-4}I^2 + 7.02 \times 10^{-4}V^2 + 8 \times 10^{-6}T^2 \\ &- 8.71 \times 10^{-4}IV - 5.1 \times 10^{-5}IT - 1.39 \times 10^{-4}VT, \end{aligned}$$

$$(4) \quad \begin{aligned} R(I,V,T) = &13.99 - 9.12 \times 10^{-2}I - 0.1283V - 5.9 \times 10^{-3}T \\ &+ 1.79 \times 10^{-4}I^2 + 3.38 \times 10^{-4}V^2 - 10^{-6}T^2 \\ &+ 3.12 \times 10^{-4}IV + 4.1 \times 10^{-5}IT + 3.8 \times 10^{-5}VT. \end{aligned}$$

The 2D sections of the 3D distributions given by the Eq. (2-4) are shown in Fig. 4. For hardfacing applications, it is desired to achieve high reinforcement by keeping weld penetration and dilution low. The condition of low dilution ($D < 40\%$) is met for the bottom left part of the plot (Fig. 4a), corresponding to low welding current $I \leq 100$A and nozzle travel speed $V \leq 90$cm/min. This result can be explained by reduced heat input under smaller currents, which causes lower degree of substrate melting and, as a consequence, lower dilution. The penetration values below 2mm are predicted for an elliptically-shaped area are limited with welding current $I \leq 100$ and nozzle speed $V \leq 95$cm/min (Fig. 4b). For the same parameter ranges, the reinforcement features inverse dependence on both I and V, predicting the highest values for $I = 80$A and $V = 60$ cm/min (Fig. 4c). Indeed, if the heat input from a low-current plasma is insufficient for producing deep melting pool, the weld material will be rather deposited on top of the substrate, resulting in higher reinforcement.

However, while all the observed individual parameter ranges seemingly define the optimal deposition conditions as low-current welding with slow nozzle movement,

ALI TAHAEI[A], PAUL HORLEY[B], MATTIA MERLIN[A], DAVID TORRES-TORRES[B], GIAN LUCA GARAGNANI[A], ROLANDO PR

the combined response of D, P and R functions may compose more complicated picture. To address this issue, we analyzed 2D plots of a cumulative parameter defined as $C = 35R - D - 15P + 100$. The positive sign of R means that larger values of reinforcement are desirable; the negative signs by D and P reflect the preference for low dilution and penetration. The coefficients by R, P and the free term were chosen to balance the contributions of individual parameters basing on their maximum values observed in Fig. 4. We consider this choice of coefficients acceptable because the $C(I, V)$ dependence (Fig. 5) features positive values in the major part of the plot; the saturated red area in the bottom left corner of each panel corresponds to the maximum value $C > 90$, clearly showing the ranges of control parameters for which our numerical model predicts the best welding bead geometry. In all cases, the low welding currents and slow nozzle motion are preferable. Remarkably, pre-heating of the substrates limits the current values required to achieve $C > 90$: at $V = 60$cm/min and $T = 250°$C welding current should be under 110A, while at the same nozzle speed under $T = 450°$C the maximum welding current is about 95A (Fig. 5a and 5c, respectively). This effect occurs because for higher substrate pre-heat the required thermal regime within the bead can be established with a lower heat input from the welding torch.

It is important to emphasize that the increase of pre-heat temperature changes considerably the behavior of the $C(I, V)$ dependence (Fig. 5): a narrow arched band corresponding to $20 \leq C \leq 80$ observed for low T (Fig. 5a) changes into a fan-shaped area embracing almost the entire area of the plot under elevated T (Fig. 5c). This means that, as long as moderate values of C are acceptable, the welding with fast nozzle motion $V > 100$cm/min can be carried out for the currents varying in wide ranges. For a slow-moving nozzle, a precise control of welding current is required. This result is of importance for fast-welding applications. In the present study, we focused on the case of low welding currents, addressing in detail the effect of sample pre-heat temperature on the parameters of welding bead.

3.2. **Characterization of optimized samples.** Analysis of parameter response surfaces showed that one of the samples in the grid was obtained within the optimized parameter area with $I = 86$A, $V = 85$cm/min and $T = 350°$C. Figure 6 presents weld bead macrostructure and the corresponding hardness profile with the average micro-hardness of the substrate is around 790 HV and that of the weld bead is 780 HV. Remarkably, the hardness of the HAZ also remains in the same ranges lacking the abrupt variation characteristic to the samples illustrated in Fig. 3. This uniformity of hardness ensures good metallurgical bond and enhanced mechanical properties of hardfacing. The carbide grains further improve the hardness of the bead matrix reaching the values of 1850 HV.

The automated Vickers Hardness profiles (Figs. 3 and 6) were measured with indentation marks spaced at 100 μm, providing a general estimation of the bulk mechanical properties because the measurement points fall over different phases inside the material. For a more refined study, we performed nano-indentation analysis of the optimized sample focusing on individual phases observed in scanning probe microscopy (Fig. 7a-c). The most representative structural formations in the bead matrix are large dendrites (Fig. 7b) and carbide grains (Fig. 7c). To diminish point-to-point variation of the measured data, we performed at least ten nano-indentation tests for different spots within the same phase in accordance to Oliver and Pharr method[21]. The nano-indentation of bead matrix material (Fig. 7d)
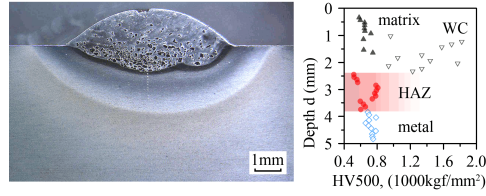
FIGURE 6. Micrograph of hardfacing deposited with $I = 86$ A, $V = 85$ cm/min and $T = 350°$C. The right panel shows the corresponding hardness profile.
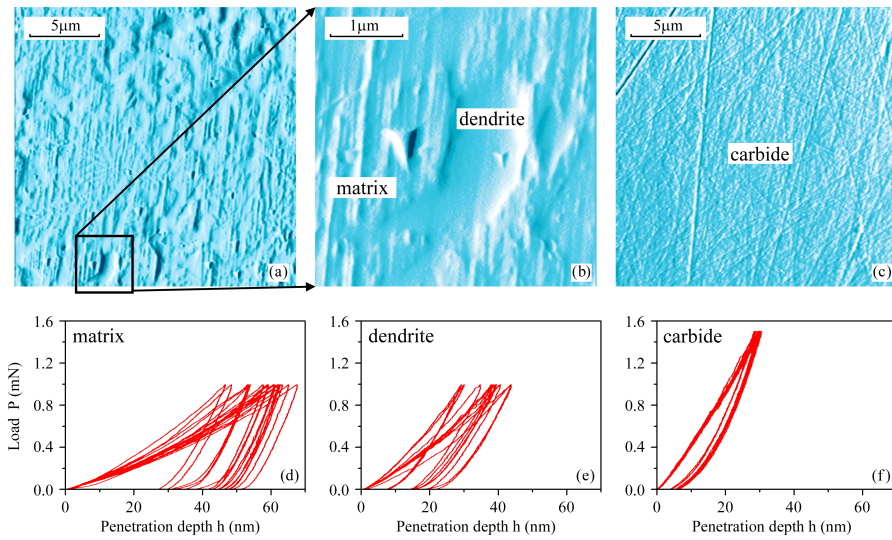

FIGURE 7. Scanning probe microscopy images of the optimized sample: a) representative sample surface, b) zoomed-in section showing the main phases and c) close-up to a tungsten carbide particle. The bottom panels provide nano-indentation curves for d) bead matrix, e) dendrite structure and f) carbide grain.

resulted in effective elastic modulus $E_r = 196 \pm 25$GPa and hardness $H = 6 \pm 3$GPa. The dendrite formations feature wide branches measuring around 3 μm long and up to 1 μm wide, respectively (Fig. 7b). The load-displacement curves for this phase (Fig. 7e) have high scattering due to low material homogeneity, resulting in effective elastic modulus $E_r = 217 \pm 64$GPa and hardness $H = 13 \pm 7$GPa. The difference in mechanical properties between the bead matrix and the dendrite phase is clearly visualized by the contrast of indentation mark sizes produced by application of the same load (Fig. 7b). The tungsten carbide particles (Fig. 7c, f) yield the highest effective elastic modulus of $E_r = 423.74 \pm 26.52$GPa and hardness of $H = 28.08 \pm 2.73$GPa. The corresponding load-displacement curves show low scattering and the lowest disparities among all three phases characterized.

ALI TAHAEI[A], PAUL HORLEY[B], MATTIA MERLIN[A], DAVID TORRES-TORRES[B], GIAN LUCA GARAGNANI[A], ROLANDO PR

To identify chemical composition of the characteristic phases within a welding bead, we used combined SEM/EDXS technique. To emphasize the structural enhancement, we illustrate side-by-side the microstructure of non-optimized and optimized samples (Fig. 8). The three prominent phases detected in scanning probe microscopy are clearly seen in SEM (Fig. 8, phases 1-3): large carbide grains and secondary dendrites embedded into a bead matrix (which by itself has ultra-fine dendrite structure that was not the main object of study of the present paper). The large grains of primary carbides (Fig. 8, phase 1) survive the welding cycle, ending up embedded in the matrix (Fig. 8, phase 1). Under the action of high temperatures the surface layer of these grains becomes partially smoothed, which can be clearly detected by comparing the micrographs in Fig. 8 with that of the original powder (Fig. 1a). The internal cavities of WC grains disappear in smaller embedded carbide particles, supporting the suggestion of partial tungsten melting during the PTAW cycle. Under these conditions, some of the small carbide particles can melt completely, producing the secondary carbide α-W_2C phase upon re-solidification. As shown in Ref. [4], the higher carbide dissolution degree in the microstructure leading to reduced hardness of the coatings occurs when higher plasma current and shielding gas flow are used. The degree of carbide dissolution depends on heat input during bead formation. The partial melting of the primary tungsten carbides triggers formation of the secondary carbides (Fig. 8, phase 2) surrounding the WC particles as feather-shaped dendrites. From the EDXS data (Table 2) one can see that the closest stoichiometric composition of these dendrites is $(Cr, Ni)_3W_3C$[8]. The growth of the secondary dendrites is more pronounced in the areas enclosed by WC grains due to the higher contents of dissolved tungsten (Fig. 8a). Depending on solidification rate, the length of these secondary dendrites may vary. We were unable to detect any explicit correlation between tungsten dissolution degree and presence of specific alloy additives because the content of both Cr and C increased in a similar proportion for every alloy. The matrix of the bead (Fig. 8, phase 3) is composed by soft $\gamma-Ni$ dendrites (350 HV) together with $\gamma-Ni+Ni_3B$ lamellar eutectic phase (500 to 800 HV) [8]. The boron required for formation of the hard Ni_3B phases comes from the filler powder[10].

Comparing the corresponding panels of Fig. 8, one can see that the optimized sample benefit from uniform distribution of carbide grains positively influencing the growth of $(Cr, Ni)_3W_3C$ dendrites. Shorter dendrite branches point to faster solidification of the optimized sample. This mechanism leads to formation of numerous (but isolated) dendrite nucleation sites homogeneously distributed in the bead matrix, forming a mixture of the different phases that improves wear resistance and strength of the material. The improvement of PTAW process efficiency can be illustrated by noting more pronounced primary carbide melting in the optimized sample under lower heat input ($I = 86$ A and $V = 85$ cm/min) in comparison to that of non-optimized sample ($I = 100$ A and $V = 70$ cm/min).

To identify the main crystalline phases composing the reinforcement layer, we conducted XRD analysis in addition to the EDXS studies reported above. The resulting spectra (Fig. 9) reveal a number of phases that were not observed in point EDXS measurements. As one can see from the figure, the welding bead contains W_2C, WC, Cr_3Si Ni_2B and FeNiCr. Though tungsten enters into the both semicarbide W_2C and mono carbide WC, the concentration of the former is considerably lower than that of the latter, judging from the XRD peak intensities. The main
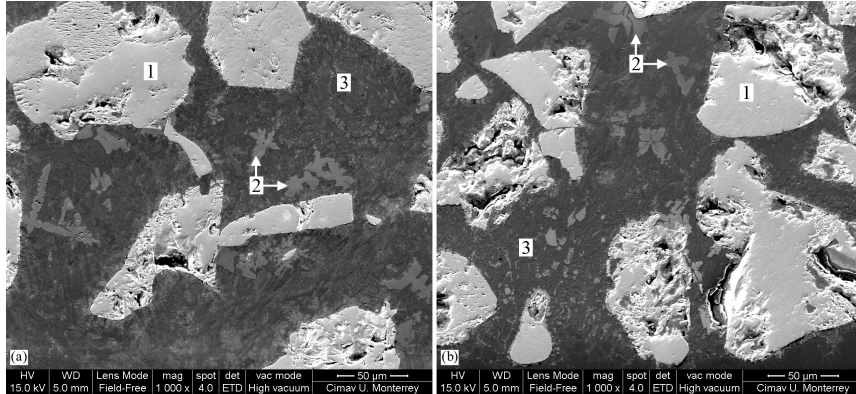
FIGURE 8. Comparison of microstructure between a) non-optimized and b) optimized welding beads obtained with $I = 100A$, $V = 70\text{cm/min}$, $T = 250°C$ and $I = 86A$, $V = 85\text{cm/min}$ and $T = 350°C$, respectively. The main structural phases are: (1) tungsten mono carbide, (2) $(Cr, Ni)_3W_3C$ dendrite formations produced by eutectic reactions, (3) nickel matrix overlay. The chemical composition of these phases is provided in Tables 2 and 3.

TABLE 2. EDXS chemical composition (Wt%) of the four phases identified in Fig. 8a for the non-optimized sample

Element	Phase 1	Phase 2	Phase 3
C K	6.72	4.11	4.64
V K	–	0.63	–
Cr K	–	13.97	17.44
Fe K	–	8.09	46.72
Ni K	–	20.14	14.41
Mo L	–	1.18	0.45
W M	93.28	48.41	16.18
Si K	–	3.47	0.16
Total	100.00	100.00	100.00

TABLE 3. EDXS chemical composition (Wt%) of the four phases identified in Fig. 8b for the optimized sample

Element	Phase 1	Phase 2	Phase 3
C K	5.96	3.99	1.07
V K	–	–	–
Cr K	–	15.15	4.24
Fe K	–	9.61	36.20
Ni K	–	21.08	51.79
Mo L	–	1.00	–
W M	94.04	45.30	3.93
Si K	–	3.87	2.77
Total	100.00	100.00	100.00

phase representing the bead matrix is the solid solution FeNiCr. The dendrites of $(Cr, Ni)_3W_3C$ observed in the SEM did not appear in the XRD data because they predominantly form at the bottom of the weld basin, which for prepared sample geometry was outside of the XRD detector range.
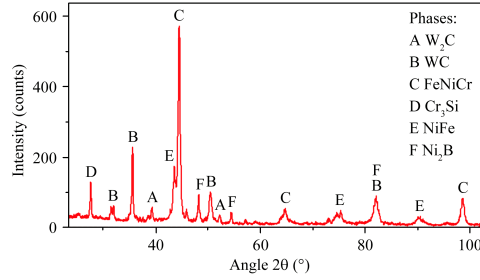
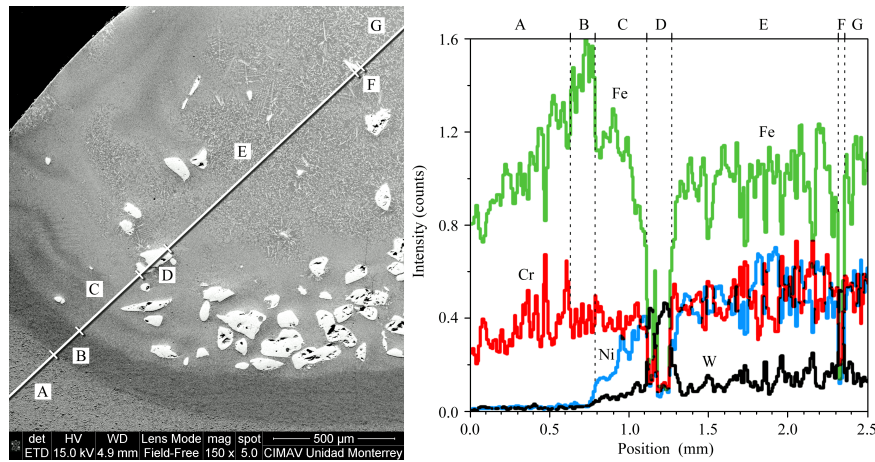FIGURE 9. XRD spectrum of the optimized sample shown in Fig.6, measured at the longitudinal section.

FIGURE 10. Close-up to the weld bead section (left panel) deposited on non-heated substrate. The composition profile (right panel) was measured along the line with the letters denoting the characteristic phases: A) heat-affected zone of the substrate; B) solidified pool of iron; C) solidified traces of weld flows; D, F) WC carbide grains; E, G) the main weld body with FeNiCr dendrites.

To gain an insight into the influence of substrate pre-heat on bead quality, we first prepared a set of reference samples with hardfacing applied over non-heated substrates using optimized parameters $I = 80$ A and $V = 60$ cm/min. The cross-section of typical hardfacing (Fig. 10) displays a "pillow" between the bead and the substrate, which is clearly distinguishable by different texture and tone in the secondary electron SEM micrograph. The interior of the bead is markedly non-homogeneous: there is a large number of fine dendrites in the upper part of the bead and there is a developed lamellar structure at the bottom of the welding pool. To clarify the nature of these phases, we performed chemical profiling along several straight segments inside the bead, illustrated by a characteristic example in the right panel of Fig. 10. The area A corresponds to heat-affected zone of the substrate featuring refined martensitic structure. The general trend in this
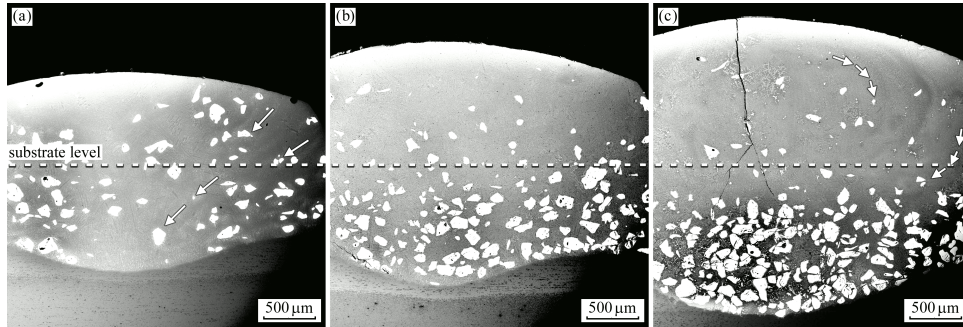
FIGURE 11. Close-up images of transversal bead sections showing the solidified flow patterns in the welding material (marked in part with white arrows) that influenced the final distribution of the carbide grains. SEM images are taken at 20kV BEC, ×30 magnification. The panels correspond to different substrate pre-heat temperatures: a) $T = 250°C$, b) $T = 350°C$, and c) $T = 450°C$. The images are aligned at the substrate level that is marked with a white dashed line.

region is incrementing iron content towards the welding pool. The maxima of Cr concentration are aligned with the minima of Fe concentration. The "pillow" region B is characterized with high iron concentration. To our opinion, the formation of this area can be attributed to a lower melting temperature of iron in comparison with that other elements found in the bead and D2 tool steel, so that a pool of iron can endure in the molten state the entire welding and most of solidification process. Inside the bead, one observes quick increase of Ni concentration starting from the metallurgic boundary, matched by increasing concentrations of Cr and W (Fig. 10c). The considerable tungsten concentration outside of carbide particles (compare Fig. 10, areas D and E) points towards partial melting of carbide grains, followed by subsequent mixture of tungsten with other elements of the bead. The smoother outlines of WC particles (Fig. 8) compared to their original rough surface (Fig. 1a) confirms this. The most important observation, to our opinion, is the formation of a lamellar structure at the bead boundary that is directly associated with carbide grains, seemingly marking the trajectories along which these particles were moving inside the molten bead. According to the composition profile (Fig. 11, right panel, area C), the darker areas of the flow patterns are richer in Fe; the minima of iron concentration correspond to the peaks of Ni concentration. Thus, the sequence of darker and brighter stripes in the SEM image represents flow lines with predominant content of the substrate material (Fe) and the welding powder material (Ni), correspondingly.

Performing bead deposition at different substrate pre-heat temperatures, we obtained the characteristic cross-sections illustrated in Fig. 11. We would like to remark that for several cross-sections prepared from the weld sample with pre-heat temperature of 450°C we have chosen the one with the clearest flow pattern image (Fig. 11c). Unfortunately, the same section also includes a crack in the bead, but it was decided in favor of keeping this image as the best illustration of flow patterns at high surface pre-heat. As one can see from the figure, there is a marked change

in the melt flow patterns obtained with different surface pre-heat temperatures: at $T = 250°C$ the flow patterns are mostly linear (Fig. 11a), at moderate pre-heat $T = 350°C$ the flow patterns are barely distinguishable at all (Fig. 11b), and at high pre-heat $T = 450°C$ the flow patterns can be seen as curling rather than linear (Fig. 11c). We attribute this variation of flow dynamics to the changes of bead profile and temperature regime of solidification. At low pre-heat, the plasma heats the substrate, melting out more material from the center of the welding pool so that the bead profile acquires a characteristic U-shape. The carbide particles of different sizes are carried upwards by the flow of molten metal and gradually settle down. The forward motion of the welding torch causes the longitudinal component of liquid metal flow, so that the trajectories of carbide grains shift to the center of the bead (Fig. 11a). Increase of substrate temperature forms deeper welding pool and keeps the bead in a molten state for a longer time, disrupting linear flow pattern. Thus, for pre-heat $T = 350°C$ the flow patterns are so weak that they are barely discernable (Fig. 11b). Finally, at high pre-heat ($T = 450°C$) both the depth of the melting pool and the solidification time increases to a degree that WC particles have sufficient time to travel to the bottom of the melting pool due to their higher density. Only a few small carbide particles remain in the upper part of the bead, dragged by circulating metal flow (Fig. 11c).

Therefore, the substrate pre-heat temperature considered as a single parameter T in reality has a multifold impact. It influences the depth of the welding pool, the profile of the bead bottom and also changes solidification time. All these parameters are of crucial importance to solidification dynamics, establishing different types of melt flow and defining the time at which the melt becomes too viscous to allow motion of the carbide grains. As one can see from the Fig. 11, despite the original hypothesis considering that highest pre-heat temperatures would be better for reduction of thermal stress of the substrate, it resulted that lower pre-heat is actually more beneficial by ensuring linear metal flow mode creating homogeneous distribution of carbide particles within the bead, which improves the hardfacing quality. In the case when no surface pre-heat was applied (Fig. 10, left panel) the traces of the metal flow are seen only at the bottom of the melting pool, without covering the entire bead cross-section, so that carbide particles are mostly clustered at the bottom of the bead. Comparing different temperature regimes illustrated in Figs. 10 and 11, one can see that the sample produced under moderate pre-heat ($T = 250°C$, Fig. 11a) features most uniform distribution of carbide grains.

4. Conclusions

The hardfacing technique using Ni-WC composite filler powder was optimized using design of experiments methodology for the PTAW process. It was shown that the best bead properties on D2 tool steel in terms of reinforcement and dilution can be achieved under low welding current $I \leq 100A$ and slowly-moving nozzle, $V \leq 90cm/min$. The numerical predictions suggested that lower substrate preheat can further improve the bead parameters. The detailed characterization of the optimized samples shown that the welding cycle leads to partial melting of carbide particles, with formation of secondary carbides phases $(Cr, Ni)_3W_3C$ with dendritic morphology, which nucleate predominantly in the vicinity of the WC primary grains. The mechanical properties of the welding bead benefit much from the

presence of the secondary dendrites that on one hand, has the intermediate hardness values between those of the bead matrix and hard carbide phase, and, on the other hand, due to their morphology, provide enhanced interlocking between the phases. The distribution of the primary carbides in the weld bead is subject to a complex melt dynamics in the welding pool. Our studies revealed the traces of melt flow patterns, detectable as lamellar structures with predominance of Fe (substrate material) and Ni (welding powder material), which are closely associated with the primary carbide grains. Without surface pre-heat, these lamellar structures are formed at the base of the bead, with the majority carbide particles agglomerated there. With a moderate pre-heat of 250°C, the geometry of the melting pool and the increased solidification time contribute to linear melt flow, ensuring the homogeneous distribution of WC particles. The increase of pre-heat to 450°C keeps the bead in liquid state for a larger time, so that heavier carbide grains end up at the bottom of the melting pool, degrading the overall mechanical performance of the bead. These results are of considerable importance for further PTAW hardfacing optimization with high prospective for a wide range of industrial applications.

5. Acknowledgments

References

[1] P.K. Siva, R.C. Srinivasa, and R.D. Nageswara: Journal of Mechanical Engineering and Technology, 2012, vol. 4, pp. 35-59.
[2] P.F. Mendez, N. Barnes, K. Bell, S.D. Borle, S.S. Gajapathi, S.D. Guest, H. Izadi, A.K. Gol, and G. Wood: Journal of Manufacturing Processes, 2014, vol. 16, pp. 4-25.
[3] S.H. Nikam, N.K. Jain, and S. Jhavar: Journal of Materials Processing Technology, 2016, vol. 230, pp. 121-130.
[4] E. Gruzdys and Š. Meškinis: Materials Science (Medžiagotyra), 2011, vol. 17, pp. 140-144.
[5] V. Vergara Díaz, J.C. Dutra, and A.S. Climaco D'Oliveira: Arc Welding, InTech Europe, Rijeka, 2011, pp. 3-20.
[6] C. Katsich and E. Badisch: Surface and Coatings Technology, 2011, vol. 206, pp. 1062-1068.
[7] A. Zikin, E. Badisch, I. Hussainova, C. Tomastik, and H. Danninger: Surface and Coatings Technology, 2013, vol. 236, pp. 36-44.
[8] T. Liyanage, G. Fisher, and A.P. Gerlich: Wear, 2012, vol. 274-275, pp. 345-354.
[9] J.F. Flores, A. Neville, N. Kapur, and A. Gnanavelu: Wear, 2009, vol. 267, pp. 213-222.
[10] A. Zikin, I. Hussainova, C. Katsich, E. Badisch, and C. Tomastik: Surface and Coatings Technology, 2012, vol. 206, pp. 4270-4278.
[11] K. Gurumoorthy, M. Kamaraj, K. Prasad Rao, A. Rao Sambasiva, and S. Venugopal: Materials Science and Engineering A, 2007, vol. 456, pp. 11-19.
[12] P.K. Siva, R.Ch. Srinivasa, and R.D. Nageswara: J. of the Braz. Soc. of Mech. Sci. and Eng., 2012, vol. 34, pp. 75-81.
[13] S. Iio, Ch. Just, and F. Xhiku: Materials and Design, 2012, vol. 33, pp. 459-468.
[14] D.E. Bhaskarananda and S. Mukherjee: International Journal of Modern Engineering Research, 2013, vol. 3, pp. 1330-1335.
[15] K. Siva, N. Murugan, and V.P. Raghupathy: Archives of Computational Materials Science and Surface Engineering, 2009, vol. 1, pp. 174-182.
[16] C.S. Wu, L. Wang, W.J. Ren, and X.Y. Zhang: Journal of Manufacturing Processes, 2014, vol. 16, pp. 74-85.
[17] S. Jhavar, N.K. Jain, and C.P. Paul: Journal of Materials Processing Technology, 2014, vol. 214, pp. 1102-1110.

ALI TAHAEI[A], PAUL HORLEY[B], MATTIA MERLIN[A], DAVID TORRES-TORRES[B], GIAN LUCA GARAGNANI[A], ROLANDO PR

[18] X.H. Wang, M. Zhang, Z.D. Zou, and S.Y. Qu: Materials Science and Technology, 2006, vol. 22, pp. 193-198.
[19] F. García-Vázquez, A. Aguirre, A. Arizmendi, H.M. Hernández-García, L. Santiago-Bautista, J. Acevedo, and B. Vargas-Arista: Materials Science Forum, 2013, vol. 755, pp. 39-45.
[20] K. Siva and N. Murugan: Procedia Engineering, 2013, vol. 64, pp. 1147-1156.
[21] W.C. Oliver and G.M. Pharr: J. Mater. Res., 1992, vol. 7, pp. 1564-1580.